

This is an electronic reprint of the original article. This reprint may differ from the original in pagination and typographic detail.

Engineering of SPECT/Photoacoustic Imaging/Antioxidative Stress Triple-Function Nanoprobe for Advanced Mesenchymal Stem Cell Therapy of Cerebral Ischemia

Yao, Minghua; Shi, Xiaojing; Zuo, Changjing; Ma, Ming; Zhang, Lu; Zhang, Hongbo; Li, Xin; Yang, Guo-Yuan; Tang, Yaohui; Wu, Rong

Published in:
ACS Applied Materials & Interfaces

DOI:
[10.1021/acsami.0c10500](https://doi.org/10.1021/acsami.0c10500)

Published: 26/08/2020

Document Version
Accepted author manuscript

Document License
CC BY

[Link to publication](#)

Please cite the original version:

Yao, M., Shi, X., Zuo, C., Ma, M., Zhang, L., Zhang, H., Li, X., Yang, G.-Y., Tang, Y., & Wu, R. (2020). Engineering of SPECT/Photoacoustic Imaging/Antioxidative Stress Triple-Function Nanoprobe for Advanced Mesenchymal Stem Cell Therapy of Cerebral Ischemia. *ACS Applied Materials & Interfaces*, 12(34), 37885-37895. <https://doi.org/10.1021/acsami.0c10500>

General rights

Copyright and moral rights for the publications made accessible in the public portal are retained by the authors and/or other copyright owners and it is a condition of accessing publications that users recognise and abide by the legal requirements associated with these rights.

Take down policy

If you believe that this document breaches copyright please contact us providing details, and we will remove access to the work immediately and investigate your claim.

Engineering of SPECT/Photoacoustic Imaging/Antioxidative Stress Triple-Function Nanoprobe for Advanced Mesenchymal Stem Cell Therapy of Cerebral Ischemia

Minghua Yao,[#] Xiaojing Shi,[#] Changjing Zuo,[#] Ming Ma,^{*} Lu Zhang, Hongbo Zhang, Xin Li, Guo-Yuan Yang, Yaohui Tang,^{*} and Rong Wu^{*}

AUTHOR INFORMATION

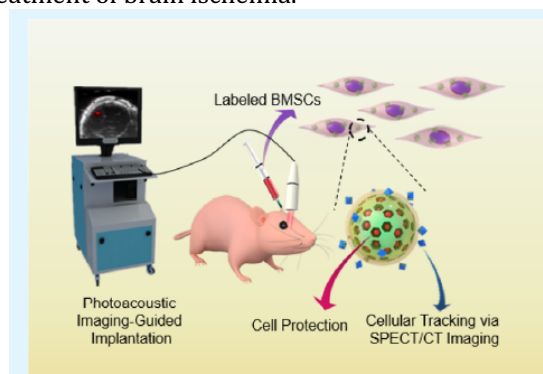
Corresponding Authors

Ming Ma – State Key Laboratory of High Performance Ceramics and Superfine Microstructures, Shanghai Institute of Ceramics, Chinese Academy of Sciences, Shanghai 200050, China; orcid.org/0000-0002-1068-4528; Email: mma@mail.sic.ac.cn Yaohui Tang – Med-X Research Institute and School of Biomedical Engineering, Shanghai Jiaotong University, Shanghai 200030, China; orcid.org/0000-0002-9603-2650; Email: yaohuitang@sjtu.edu.cn Rong Wu – Department of Medical Ultrasound, Shanghai General Hospital, School of Medicine, Shanghai Jiaotong University, Shanghai 200080, China; Email: wurong7111@163.com

Authors

Minghua Yao – Department of Medical Ultrasound, Shanghai General Hospital, School of Medicine, Shanghai Jiaotong University, Shanghai 200080, China Xiaojing Shi – Med-X Research Institute and School of Biomedical Engineering, Shanghai Jiaotong University, Shanghai 200030, China Changjing Zuo – Department of Nuclear Medicine, Changhai Hospital, The Second Military Medical University, Shanghai 200433, China; orcid.org/0000-0002-2051-766X Lu Zhang – Department of Nuclear Medicine, Changhai Hospital, The Second Military Medical University, Shanghai 200433, China; orcid.org/0000-0001-7049-0760 Hongbo Zhang – Pharmaceutical Sciences Laboratory and Turku Bioscience Centre, Åbo Akademi University, FI-20520 Turku, Finland; orcid.org/0000-0002-1071-4416 Xin Li – Department of Medical Ultrasound, Shanghai General Hospital, School of Medicine, Shanghai Jiaotong University, Shanghai 200080, China Guo-Yuan Yang – Med-X Research Institute and School of Biomedical Engineering, Shanghai Jiaotong University, Shanghai 200030, China

ABSTRACT: The precise transplantation, long-term tracking, and maintenance of stem cells with maximizing therapeutic effect are significant challenges in stem cell-based therapy for stroke treatment. In this study, a unique core-shell labeling nanoagent was prepared by encapsulating a cobalt protoporphyrin IX (CoPP)-loaded mesoporous silica nanoparticle (CPMSN) into a ¹²⁵I-conjugated/spermine-modified dextran polymer (¹²⁵I-SD) by microfluidics for mesenchymal stem cell (MSC) tracking and activity maintenance. The CPMSN core not only exhibits excellent photoacoustic (PA) imaging performance induced by the intermolecular aggregation of CoPP within the mesopores but also protects the MSCs against oxidative stress by sustained release of CoPP. Meanwhile, the addition of a ¹²⁵I-SD shell can increase the uptake efficiency in MSCs without inducing cell variability and enable the single-photon-emission computed tomography (SPECT) nuclear imaging. In vivo results indicated that CPMSN@¹²⁵I-SD labeling could allow for an optimal combination of instant imaging of MSCs, with PA to guide intracerebral injection, followed by multiple time point SPECT imaging to consecutively track the cell homing. Importantly, the sustained release of CoPP from CPMSN@¹²⁵I-SD significantly increased the survival of MSCs after injection into an ischemic mouse brain and promoted neurobehavioral recovery in ischemic mice. Thus, CPMSN@¹²⁵I-SD represents a robust theranostic probe for both MSC tracking and maintaining their therapeutic effect in the treatment of brain ischemia.



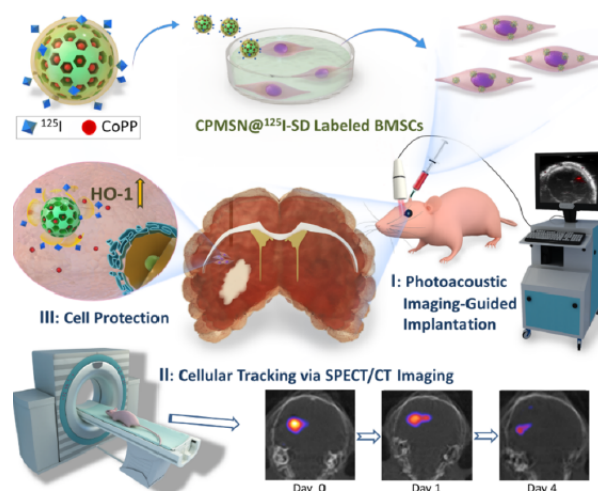
KEYWORDS: theranostic, mesoporous silica, brain ischemia, cell labeling, stem cell therapy

INTRODUCTION

Stroke is the second leading cause of death and the first leading cause of serious disabilities worldwide but with very few effective therapies. During the last decade, transplantation of exogenous stem cells has shown encouraging initial results for the treatment of ischemic stroke.¹⁻⁴ Nevertheless, its clinical transformation is markedly limited because of low cell implantation accuracy, lack of adequate imaging techniques for monitoring cell homing and engraftment, and low survival rate of the transplanted stem cells.⁵⁻⁷ Research activities in stem cell nanotechnology have flourished in recent years, and different nanoparticle-based labeling agents have been employed to monitor the biological process or improve the therapeutic accuracy of stem cell therapy for ischemic stroke.⁸⁻¹¹ For instance, the typical photoacoustic (PA) contrast agents, Prussian blue nanoparticles and semiconducting polymer nanoparticles, have proven to be effective in stem cell labeling and real-time PA imaging-guided cellular injection in the mouse brain.^{8,12} Besides, superparamagnetic iron oxide nanoparticles have been successfully employed in the tracking of transplanted stem cells via magnetic resonance imaging (MRI) for monitoring their migration to the affected neurological locus in cerebral ischemia.¹³ Despite being promoted by the advancements of these cell labeling-based imaging modalities, stem cell therapy still suffers from compromised therapeutic efficacy owing to the rapid cell death induced by excessive oxidative stress and/or inflammation in the ischemic microenvironment.^{14,15} In line with this notion, development of an effective imaging nanoprobe with an antioxidant protective effect will be greatly beneficial for stem cell therapy. In addition, instant imaging of stem cells at the time of delivery can significantly improve the accuracy of cell transplantation, while high-resolution, longitudinal cellular tracking after transplantation can help to determine the efficacy of stem cell therapy and the level of cell engraftment, both of which are crucial to the success of stem cell therapy.^{16,17} Nevertheless, these two demands cannot be simultaneously satisfied by the current single-modality imaging techniques because of the inherent technical limitations.^{18,19} For example, PA and ultrasound (US) imaging possess significant advantages in real-time guiding stem cell implantation owing to its high contrast, high flexibility, and fast data acquisition capability, whereas their spatial resolution is greatly limited by the acoustic wavelength.²⁰⁻²⁵ MRI with anatomical imaging resolution and single-photon-emission computed tomography (SPECT) with high sensitivity and quantitative capability are the preferred methods for long-term monitoring of cell distribution and migration in vivo.²⁶ However, neither MRI nor SPECT imaging is suitable for instant imaging because of their long data acquisition time.²⁷ Thus, to acquire effective stem cell imaging both during and after stem cell transplantation, there is an imperative need for an ideal imaging nanoprobe, which possesses all the technical features required for both treatment stages. Accordingly, we herein propose an all-in-one labeling strategy based on a novel theranostic nanoprobe that enables instant imaging at the time of stem cell transplantation, as well as longtime tracking of its migration and improving its survival after transplantation into an ischemic mouse brain ([Scheme 1](#)). This theranostic probe has a unique core-shell structure with cobalt protoporphyrin IX (CoPP)-loaded mesoporous silica nanoparticles (CPMSNs) as the core and the ¹²⁵I-conjugated/ spermine-modified dextran polymer (¹²⁵I-SD) as the shell (CPMSN@¹²⁵I-SD), which is constructed with the aid of a microfluidic nanoprecipitation strategy. In this nanoplatform, the CPMSNs exhibit superior PA imaging ability based on a mesopore-induced aggregation effect and can be employed to label bone marrow stromal cells (BMSCs) for real-time PA imaging-guided transplantation into the mouse brain. The ¹²⁵I-SD shell not only increases the labeling efficiency and biosafety of CPMSNs toward stem cells but also enables us to quantitatively track stem cells under SPECT imaging after transplantation. In addition, the sustained release of CoPP can protect the stem cells against oxidative stress. Moreover, we systemically studied the effects and underlying mechanism of CPMSN@¹²⁵I-SD-labeled BMSCs for stroke treatment.

Scheme 1. Schematic Illustrating the Triple Functionality of CPMSN@¹²⁵I-SD for Stem Cell Therapy of Brain Ischemia; (I) a PA Contrast Imaging Agent for Real-Time Guided Cellular Implantation; (II) a SPECT/CT

Molecular Imaging Agent for Cell Tracking after Implantation; and (III) an Antioxidative Stress Agent That Protects the Transplanted Cells in the Oxidative Microenvironment of Ischemic Brain Tissue



RESULTS AND DISCUSSION

Preparation and Characterization of CPMSNs. A heterogeneous oil–water biphasic stratification approach was used to synthesize biodegradable mesoporous silica nanoparticles (MSNs).²⁸ Transmission electron microscopy (TEM) and scanning electron microscopy (SEM) analyses revealed that the obtained MSNs possess center-radial mesopore channels and uniform particle diameters of about 101.0 nm (Figure 1a). N₂ adsorption–desorption isotherm analysis was employed to investigate the pore structure of the MSNs (Figure S1). The results revealed that the MSNs have a Brunauer–Emmet–Teller surface area of 222.7 m² g^{−1}, a pore volume of 0.86 cm³ g^{−1} (Figure S1a), and a mean pore diameter of 6.0 nm (Figure S1b). The structural features of the MSNs obtained, including their large surface area, open pore structure, and silanol-enriched pore walls, greatly facilitate the adsorption of CoPP via intermolecular hydrogen bonding interactions. Thus, CPMSNs were easily constructed by mixing pristine MSNs with a certain proportion of CoPP in ethanol solution. Our results showed that the amount of CoPP loaded onto the MSNs can be increased by adding more CoPP to the synthesis (Figure S2). The maximum CoPP loading of the MSNs is 6.4%, which is achieved with an MSN/CoPP mass feed ratio of 1.75:1.

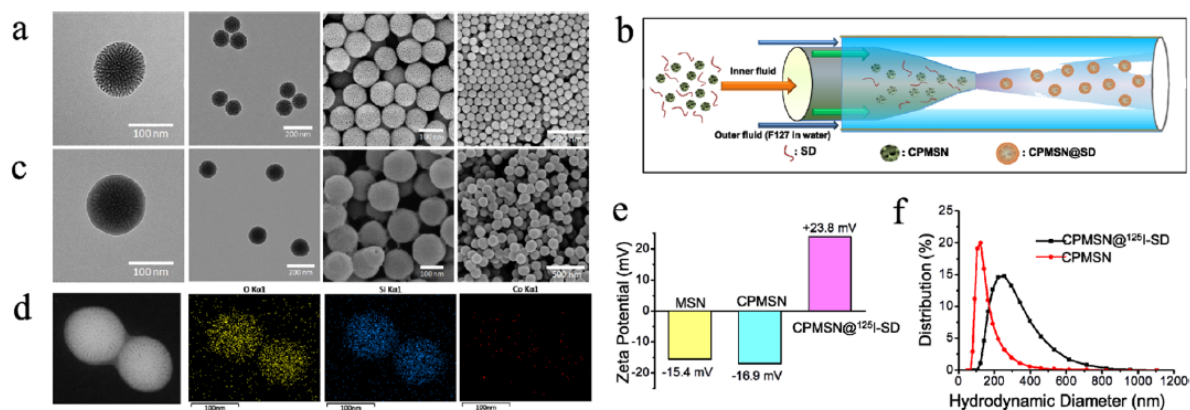


Figure 1. Microfluidic synthesis, structural characterizations, biological effect, and biodegradation of CPMSN@SD. (a) TEM and SEM images of CPMSNs fabricated by microfluidics with an SD/CPMSNs mass feed ratio of 2. (b) Schematic illustration for the microfluidic synthesis of CPMSN@SD. (c) TEM and SEM images of CPMSN@¹²⁵I-SD. (d) Dark-field (left) and element mapping images of CPMSN@SD (from left to right: O, Si, and Co). (e) Zeta potential of each particle. (f) Hydrodynamic diameter distribution of CPMSNs and CPMSN@¹²⁵I-SD.

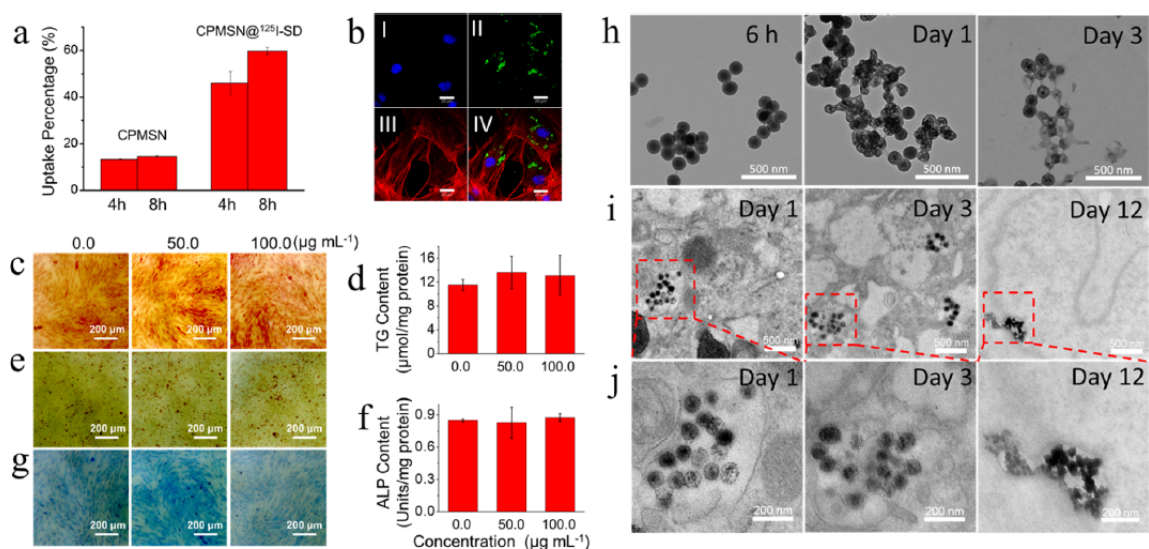


Figure 2. (a) Cell labeling efficiencies of CPMSNs and CPMSN@¹²⁵I-SD after incubation with BMSCs for 4 and 8 h. The samples were measured in parallel ($n = 3$). (b) LSCM images of FITC-conjugated CPMSN@SD in BMSCs: (I) 4',6-diamidino-2-phenylindole (DAPI)-stained cell nuclei, (II) FITC-labeled nanoparticles, (III) TRITC-phalloidin-stained f-actins, and (IV) Merged image. Scale bars = 20 μm. (c) Oil Red staining and (d) TG content of BMSCs after induction of adipogenic differentiation. (e) ALP staining and (f) corresponding ALP activity of BMSCs after induction of osteogenic differentiation. The samples were assayed in parallel ($n = 3$). (g) Toluidine blue staining of BMSCs following the induction of chondrogenic differentiation. (h) TEM images of CPMSN@¹²⁵I-SD nanoparticles after immersion in PBS for different periods of time (6 h, 1 day, and 3 days). (i,j) TEM images of CPMSN@¹²⁵I-SD within BMSCs after incubation for different time periods. The red square in each image in (i) indicates the presence of the nanoparticle aggregates in BMSCs.

Preparation and Characterization of CPMSN@¹²⁵I-SD. CPMSNs were coated with spermine-modified dextran (SD, the molecular structure and the ¹H NMR spectra of which are shown in Figure S3) via a microfluidic nanoprecipitation approach in order to provide positively charged particle surfaces to facilitate stem cell internalization. Thereinto, the SD was synthesized by conjugation of spermine to partially oxidized acetalated dextran via reductive amination.²⁹ The number-average molecular weight of the SD was measured to be 5652 Da by gel permeation chromatography (GPC) (Figure S4). Meanwhile, the mass proportion of spermine in the modified dextran is about 7.6 wt %, as derived by elemental analysis. It is worth noting that as a novel synthetic polycationic polymer, SD exhibits superior performances in biodegradability and biocompatibility in comparison with the conventional ones such as polyethyleneimine and polylysine,^{30,31} thereby acting as an excellent coating for promoting cellular uptake of nanoparticles or genetic materials.^{32,33} The microfluidics-assisted nanoassembly process was conducted using a glass-fabricated three-dimensional (3D) coaxial flow capillary platform,^{34,35} where the inner fluid (an ethanol solution containing SD and CPMSNs) flows through the inner capillary while the outer fluid (an alkaline aqueous solution containing surfactant F127) flows in the gap between the inner and outer capillaries (Figure 1b). The rapid mixing of the ethanol solution with the water solution at the inner nozzle exit site quickly decreases the solubility of the SD, driving the nucleation and formation of SD layers on the CPMSNs. As we expected, TEM and SEM analyses revealed that the pore openings on the CPMSN particle surfaces are completely covered with a dense SD layer (Figures 1c and S5). It was found that the thickness of the SD layer gradually increased with the increment of the feed ratio of SD/CPMSNs. However, the coexistence of core-shell-structured CPMSN@SD and pure SD nanoparticles was found when the mass ratio of SD/CPMSNs was increased to 4 (Figure S5). Notably, the product CPMSN@SD showed high uniformity with regard to both particle size (average diameter 139.6 nm as derived using ImageJ, Figure S6) and core-shell morphology when the feed concentrations of CPMSNs and SD were fixed at 0.25 and 0.5 mg mL⁻¹, respectively (Figure 1c). Finally, the ¹²⁵I labeling of CPMSN@SD was performed by conjugation of the polymers with ¹²⁵I in order to realize SPECT molecular imaging. The radiolabeling efficiency was measured to be about 90.0%. The labeling stability was also tested by incubating CPMSN@¹²⁵I-SD in 0.1% fetal bovine serum (FBS) solution for different periods of time. Only 11.7% loss of radioactivity incorporation was observed for CPMSN@¹²⁵I-SD after 3 days of incubation at 37 °C (Figure S7). The presence of Co in the core-shell-structured nanoparticles was clearly demonstrated by elemental mapping analysis (Figure 1d). Meanwhile, the characteristic Co 2p peaks appear at 779.8 and 795.5 eV in the X-ray photoelectron spectroscopy (XPS) spectra (Figure S8). These results confirmed the presence of CoPP in

MSNs. Furthermore, the zeta potentials of the three particles (MSNs, CPMSNs, and CPMSN@₁₂₅I-SD) obtained at different synthetic stages were measured (Figure 1e). The zeta potentials of the MSNs and CPMSNs are -15.4 and -16.9 mV, respectively, indicating that CoPP loading has a negligible effect on the surface charge of the MSNs. However, after SD coating, the particle surface charge becomes very positive (+23.8 mV), which is attributed to the high density of spermine groups in SD. In addition, as shown in Figure 1f, the mean hydrodynamic diameter of the CPMSNs is 149.4 nm while that of CPMSN@₁₂₅I-SD is increased to 283.0 nm because of the additional SD layer.

MSC Labeling. To optimize the labeling efficiency, 400 µg of CPMSN@₁₂₅I-SD nanoparticles was coincubated with BMSCs (cell number: 1,000,000) for different periods of time (4 and 8 h). The inductively coupled plasma optical emission spectrometry (ICP-OES) profile indicates that about 46.1% of the added CPMSN@₁₂₅I-SD nanoparticles are taken up by the BMSCs after 4 h, and this value increases to 59.8% upon incubation for 8 h (Figure 2a). The average amounts of CPMSN@₁₂₅I-SD in 1,000,000 BMSCs after incubation for 4 and 8 h were calculated to be about 184.0 and 239.2 µg, respectively. However, for the CPMSNs without the SD coating, the labeling ratio is only 14.6% after 8 h of incubation. The significant differences in the labeling efficiencies of CPMSN@₁₂₅I-SD and the CPMSNs indicate that the cationic polymer layer of SD significantly increases the interaction between the nanoparticles and the cell membrane, thereby facilitating their stem cell uptake. To further investigate whether CPMSN@₁₂₅I-SD nanoparticles are successfully internalized in BMSCs, laser scanning confocal microscopy (LSCM) observation was performed after 8 h of incubation. Here, the CPMSN@SD particles were conjugated with a fluorescein isothiocyanate (FITC) probe instead of ¹²⁵I to facilitate observation of their intracellular location. As shown in Figure 2b, a large proportion of green signal dots, which indicate the labeling agent, are located in the interior of the labeled BMSCs. This result clearly demonstrates that CPMSN@₁₂₅I-SD nanoparticles can successfully label BMSCs with high efficiency for stem cell tracking and therapy.

Effects of CPMSN@₁₂₅I-SD Labeling on Cell Viability and Multipotential Differentiation. The effects of CPMSN@₁₂₅I-SD on the viability and multipotential differentiation of BMSCs were evaluated to confirm its feasible application in BMSC therapy. The cell viability of BMSCs after incubation with CPMSN@₁₂₅I-SD at various concentrations in the range of 0–100 µg mL⁻¹ for 24 and 48 h was measured using the Cell Counting Kit-8 (CCK-8) assay. As shown in Figure S9, CPMSN@₁₂₅I-SD has a negligible effect on the survival of BMSCs, demonstrating that it can be safely implemented for stem cell labeling and therapy. BMSCs are pluripotent cells that can differentiate into different cell types, such as adipocytes, osteoblasts, and chondrocytes.³⁶ It is important to determine whether our newly designed nanoagent CPMSN@₁₂₅I-SD adversely affects the differentiation capability of BMSCs. Accordingly, three in vitro BMSC differentiation tests including adipogenic, osteogenic, and chondrogenic differentiations were conducted with CPMSN@₁₂₅I-SD labeling at different particle concentrations from 0 to 100 µg mL⁻¹. For adipogenic induction, both the unlabeled and labelled BMSCs were subjected to an adipogenic inducer for 21 days. The formation of lipid droplets was observed for the three cell samples by inverted microscopy (Figure 2c). Furthermore, quantification of triglyceride (TG) contents showed no obvious difference of CPMSN@₁₂₅I-SD-labeled BMSCs at each concentration compared to that of the unlabeled BMSCs (Figure 2d). The effect of CPMSN@₁₂₅I-SD labeling on osteocyte differentiation for BMSCs was further investigated using alkaline phosphatase (ALP) activity as an indicator. After 14 days of differentiation, no significant difference in ALP activity is observed between the CPMSN@₁₂₅I-SD-labeled and control groups (Figure 2e,f). Similarly, in the assessment of cartilage differentiation, the tendency for BMSCs to differentiate into chondrocytes was not affected by labeling with CPMSN@₁₂₅I-SD, as confirmed by the toluidine blue assay (Figure 2g). Thus, these results conclusively confirmed that CPMSN@₁₂₅I-SD had negligible effects on BMSC differentiation in the current study, further demonstrating its safety for stem cell-based therapy.

Material Degradability and CoPP Release. MSNs with large pore sizes and a center-radial mesostructure were employed as the core of CPMSN@₁₂₅I-SD because of their excellent degradability. As we expected, although the material structure remains intact after immersion in phosphate-buffered saline (PBS) for 6 h, an obvious structural collapse of the CPMSN cores is observed after 1 day (Figure 2h), suggesting that a considerable amount of silica has been degraded and released into the solution. Quantitatively, about 66.0 and 83.0% of the Si is released from CPMSN@₁₂₅I-SD upon 3- and 5-day immersions, respectively (Figure S10). We also confirmed that the gradual structural collapse of CPMSNs also occurs in the intracellular environment (Figure 2i,j). Remarkably, only a small number of irregular and aggregated particles are observed inside the cells after 12 days of coincubation. The dynamics of CoPP released from the labeling agent in PBS was also studied along with the in vitro material degradation. As shown in Figure S11, the CoPP release gradually increased in a time-dependent manner. The cumulative CoPP release rates were about 15.0 and 22.1% upon immersion for 3 and 5 days, respectively. Thus, the biodegradation of the inorganic CPMSN core of our nanoplatform not only ensures sustained release of the antioxidative-stress agent CoPP but also guarantees longterm material biosafety for both the transplanted BMSCs and living systems.

PA Contrast Imaging Using CPMSN@¹²⁵I-SD. PA

imaging is an advanced imaging technique that relies on the employment of laser-generated US.³⁷ This imaging modality involves NIR light excitation and combines the merits of both optical and US imaging, providing noninvasive and high-contrast deep tissue imaging.³⁸ As shown in Figure 3a, the PA signal of CPMSN@¹²⁵I-SD was clearly observed in a wide wavelength range from 680 to 860 nm when the CoPP concentration was above 9.0 μM . For all concentrations, the particles exhibited superior imaging contrast and PA signal intensity at 680 nm compared to those at longer wavelengths (Figure 3a,b). However, the PA signal at 680 nm for free CoPP in aqueous solution was very weak, even at a high concentration of 36 μM (Figure S12). Furthermore, the PA intensities of free CoPP and CPMSN@¹²⁵I-SD at 680 nm were quantitatively compared at an equivalent CoPP concentration of 36 μM (Figure S13). A 4.5-fold increase in the PA signal was observed once CoPP was loaded into CPMSN@¹²⁵I-SD. This observed enhancement in PA signal was mainly a result of the intermolecular aggregation of CoPP inside the mesopores, which significantly increased its light absorption in the NIR wavelength range.³⁹ Furthermore, the feasibility of in vivo PA imaging using CPMSN@¹²⁵I-SD was confirmed by subcutaneous injections of different numbers of labeled BMSCs (from 65,000 to 260,000 cells) into nude mice. As indicated in Figure 3c, the PA signal was gradually amplified with an increasing cell number. We also observed a linear relationship between the total PA signal and the BMSC number for in vivo PA imaging (Figure 3d), demonstrating that CPMSN@¹²⁵I-SD could be used as an efficient PA contrast agent to quantitatively label and image BMSCs during cell transplantation.

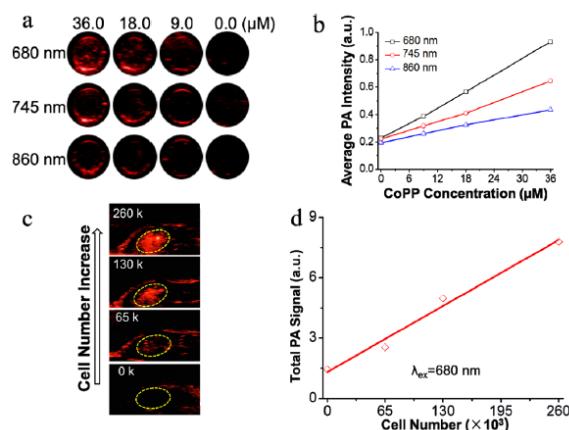


Figure 3. PA imaging of CPMSN@¹²⁵I-SD. (a,b) PA images and corresponding average intensities of CPMSN@¹²⁵I-SD with various CoPP concentrations (from 0 to 36 μM) at several wavelengths (680, 745, and 860 nm) in the NIR region. (c) PA images recorded at 680 nm and (d) the corresponding values of total PA intensity of the injection site in mice after subcutaneous injection of different numbers of the labeled BMSCs (from 0 to 260,000 cells). The PA signal intensity was calculated within the yellow ROI.

Monitoring of BMSCs by PA and SPECT/CT Imaging. Stem cell-based therapy is emerging as a promising treatment for stroke patients. However, imaging the stem cells and fully elucidating their distribution and migration behavior in real time during transplantation remain substantial challenges.⁴⁰ Several single-modal imaging agents with PA imaging capability (e.g., gold nanoparticles^{41,42} and Prussian blue nanoparticles⁸) or SPECT imaging capability (e.g., ⁶⁴Cu-PTSM, ¹¹¹In-oxiquinolone, and ^{99m}Tc-HMPAO⁴³) have been utilized as effective stem cell labeling probes in recent years. However, these single-modal imaging approaches enable the acquisition of only limited information and barely satisfy the multiple requirements for clinical application of stem cell therapy.⁴⁴ In this study, our CPMSN@¹²⁵I-SD-labeled BMSCs have been demonstrated to exhibit both high-contrast PA imaging ability and ¹²⁵I radioactivity, enabling real-time imaging-guided cellular injection via PA imaging and monitoring of the labeled BMSCs under SPECT/CT imaging. To confirm this, we evaluated the PA signal change in a murine brain after intracerebral injection of about 500,000 unlabeled and CPMSN@¹²⁵I-SD-labeled BMSCs into the periinfarct region. Figure 4a shows that no detectable PA signal is observed in the murine brain injected with unlabeled BMSCs. However, a significant enhancement of PA signal (about 10-fold increase in total signal intensity, Figure S14) at the injection site is observed upon implantation of labeled BMSCs. Furthermore, we constructed a 3DPA image of the murine brain by combining multiple 2D images of serial thin sections, from which the anatomical distribution of the PA-visible BMSCs was clearly observed (Figure 4b and Movie S1). More importantly, our findings revealed that CPMSN@¹²⁵I-SD labeling enabled sensitive PA imaging of BMSCs through an intact murine skull, highlighting its potential for real-time imaging-guided cellular transplantation in the ischemic brain. To further track the transplanted BMSCs, SPECT/CT imaging of

ischemic mice was conducted in the days following transplantation. As shown in Figure 4c, sustained radioactivity in murine brain was detected for 7 days. Importantly, it is clearly observed that, 1 day postinjection, a certain proportion of CPMSN@¹²⁵I-SD-labeled BMSCs began to migrate from the injection site to the adjacent lesion area, and the results by SPECT/CT imaging demonstrate that about 35.3 and 46.2% of the labeled BMSCs have migrated to the ischemic area at day 1 and day 3 postinjection, respectively. This result revealed that the spatial location and homing behavior of the transplanted BMSCs could be clearly monitored by SPECT/CT imaging.

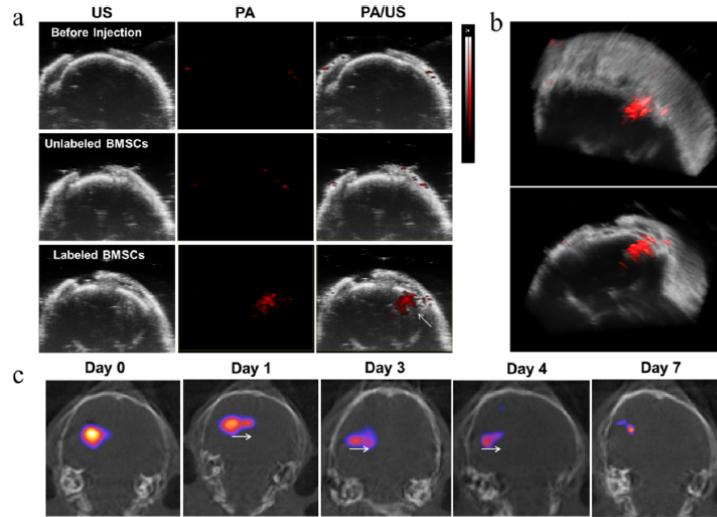


Figure 4. In vivo PA and SPECT/CT imaging of the labeled BMSCs injected in the ischemic mouse brains. (a) PA images (680 nm) of ischemic mouse brains immediately after intracerebral injection of 500,000 unlabeled or CPMSN@¹²⁵I-SD-labeled BMSCs. (b) Representative 3D reconstructed PA images of ischemic mouse brain tissue after injection of 500,000 labeled BMSCs. (c) SPECT/CT images of ischemic mouse brain tissue on different days (0–7 days) after intracerebral injection of the labeled BMSCs (500,000 cells). The white arrows show the migration direction of the labelled BMSCs.

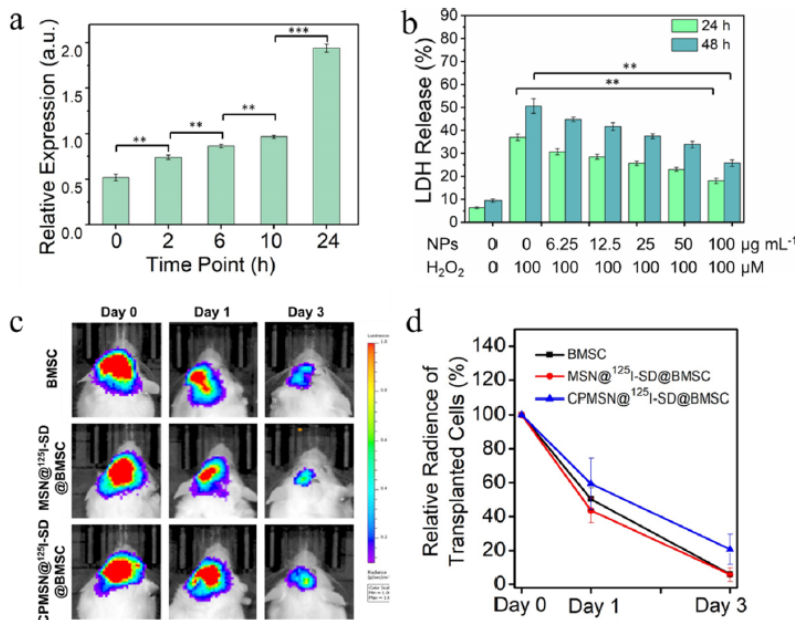


Figure 5. CPMSN@¹²⁵I-SD-enhanced BMSC survival in vitro and in vivo. (a) HO-1 expression levels of BMSCs after labeling with CPMSN@¹²⁵I-SD for different periods of time (0–24 h). The samples were assayed in parallel (n = 3). (b) Cell death assessment for BMSCs after treatment with different concentrations of CPMSN@¹²⁵I-SD (0–100 µg mL⁻¹) and exposure to 100 µM H₂O₂ for 24 and 48 h. The samples were assayed in parallel (n = 3). (c) Bioluminescence imaging of representative mice over a period of time after intracerebral injection of pLenti-3FLAG-luc2-tdTomato-transfected BMSCs with and without labeling using MSN@¹²⁵I-SD and CPMSN@¹²⁵I-SD. (d) Relative cell numbers for each mouse group (n = 4) on days 1 and 3. **P < 0.01 and ***P < 0.001.

CPMSN@₁₂₅I-SD-Enhanced BMSC Survival after Transplantation

into the Ischemic Mouse Brain. Cell survival is one of the key hindrances to the success of stem cell-based therapy for brain ischemic stroke, which is mainly due to the excessive oxidative stress and inflammation in the ischemic area.^{45,46} CoPP, a representative porphyrin derivative, is well known for its antioxidant effect by increasing the HO-1 expression of cells. In this study, the antioxidative stress effect of CPMSN@₁₂₅I-SD on labeled BMSCs was evaluated *in vitro* to confirm that the designed theranostic probe still exhibited the pharmacological effect of free CoPP. The Western blot analysis results shown in [Figures 5a](#) and [S15](#) clearly demonstrate that coincubation with CPMSN@₁₂₅I-SD markedly upregulated the HO-1 expression in BMSCs. Specifically, the level of HO-1 expression increased by 3.8-fold upon treatment with 50 $\mu\text{g mL}^{-1}$ CPMSN@₁₂₅I-SD for 24 h. HO-1 upregulation in BMSCs suggested that their antioxidative resistance may also increase. To confirm this, BMSCs treated with CPMSN@₁₂₅I-SD at concentrations from 0 to 100 $\mu\text{g mL}^{-1}$ were exposed to a serumfree medium containing 100 μM of H_2O_2 for 24 and 48 h, followed by cell death assessment using a lactate dehydrogenase (LDH) cytotoxicity assay. Here, the addition of H_2O_2 to the cell culture medium was used to mimic the reactive oxygen species-rich microenvironments of the ischemic brain. As shown in [Figure 5b](#), for each treatment time (24 h and 48 h), the relative LDH release from the cells gradually decreased with increasing nanoparticle concentration. In particular, the LDH released from the 100 $\mu\text{g mL}^{-1}$ groups was decreased by about 48.9 and 50.9% for the 24 and 48 h treatment, respectively. Thus, these results showed that our designed theranostic nanoprobe exhibited a clear antioxidative stress effect by upregulating the HO-1 expression in the labelled BMSCs. To verify that CPMSN@₁₂₅I-SD exerts the same protective function on MSCs *in vivo*, the ischemic mice were randomly divided into three groups ($n = 4$) that received intracerebral injection of PBS, MSN@₁₂₅I-SD-labeled BMSCs, or CPMSN@₁₂₅I-SD-labeled BMSCs (MSN@₁₂₅I-SD@BMSC represents BMSCs labeled with non-CoPP-loaded MSN@₁₂₅I-SD). The cells were transfected with pLenti-3FLAG-luc2- tdTomato before labeling in order to quantify the viability of the transplanted BMSCs by bioluminescence imaging. As indicated in [Figure 5c](#), bioluminescent signal was observed after injection of about 500,000 cells in the peri-infarct region of the murine brain. A dramatic reduction of the signal was observed after 3 days in each group, which indicated that a large number of the transplanted BMSCs died owing to strong oxidative stress damage. However, the relative cell viability in the CPMSN@₁₂₅I-SD@BMSCs group (15.1%) is about 2.3- and 2.09-fold higher compared to those of the non-CoPP containing groups (BMSCs and MSN@₁₂₅I-SD@BMSCs), respectively ([Figure 5d](#)). Therefore, our results indicated that intracellular labeling with CPMSN@₁₂₅I-SD can potentially be used to protect BMSCs against oxidative stress, thus promoting cell survival.

Effect of CPMSN@₁₂₅I-SD-Labeled BMSCs on Neurobehavioral Recovery.

Cresyl violet staining and behavioral tests were performed to evaluate the effects of BMSCs on brain atrophy and neurobehavioral recovery after stroke. We found that, compared to the PBS group, injection of BMSCs reduced atrophy volume by about 30%, while injection of CPMSN@₁₂₅I-SD-labeled MSCs reduced atrophy volume by about 50% ([Figure 6a,b](#)). Previous studies have demonstrated the beneficial role of MSCs in neurobehavioral recovery in mice subjected to ischemic stroke.⁴⁷ Similarly, in the present study, mice treated with BMSCs showed better performance in typical motor and cognitive tests. Interestingly, transplantation of CPMSN@₁₂₅I-SD-labeled BMSCs substantially improved the neurobehavioral recovery of mice at 14 days after stroke, as assessed by the modified neurological severity score (mNSS) ([Figure S16](#)) and the Rotarod test ([Figure S17](#)), as well as the Smart cage test ([Figure 6c,d](#)), suggesting that increasing the survival of BMSCs with CPMSN@₁₂₅I-SD may contribute to neurobehavioral recovery of stroke mice.

It is well documented that MSCs exert their neurorestorative effects by increasing angiogenesis and neurogenesis via their paracrine effects.⁴⁸ Accordingly, in this study, we counted the number of CD31⁺ microvessels in the peri-infarct region of striatum and DCX⁺ neuroblast in subventricular zone (SVZ) in ischemic mouse brains. To count CD31⁺ vessels, the field in the peri-infarct area was imaged per brain section and then 3Dreconstructed using a confocal microscope ([Figure 6e,f](#)). Meanwhile, the number of DCX⁺ cells in the SVZ was measured based on the area of the fluorescence signal and quantified as the ipsilateral to contralateral ratio using Image J software ([Figure 6g,h](#)). We found that BMSC treatment increased angiogenesis and neurogenesis, and injection of CPMSN@₁₂₅I-SD-labeled BMSCs further enhanced angiogenesis and neurogenesis and thus promoted neurobehavioral recovery in stroke mice. To investigate the underlying mechanisms of BMSC-induced angiogenesis and neurogenesis, we monitored the expression of vascular endothelial growth factor (VEGF), an important angiogenesis and neurogenesis mediator during the recovery process,⁴⁹ by Western blot analysis ([Figure S18](#)). The results showed that transplantation of CPMSN@₁₂₅I-SD-labeled BMSCs significantly upregulated the VEGF expression, further increasing angiogenesis and neurogenesis.

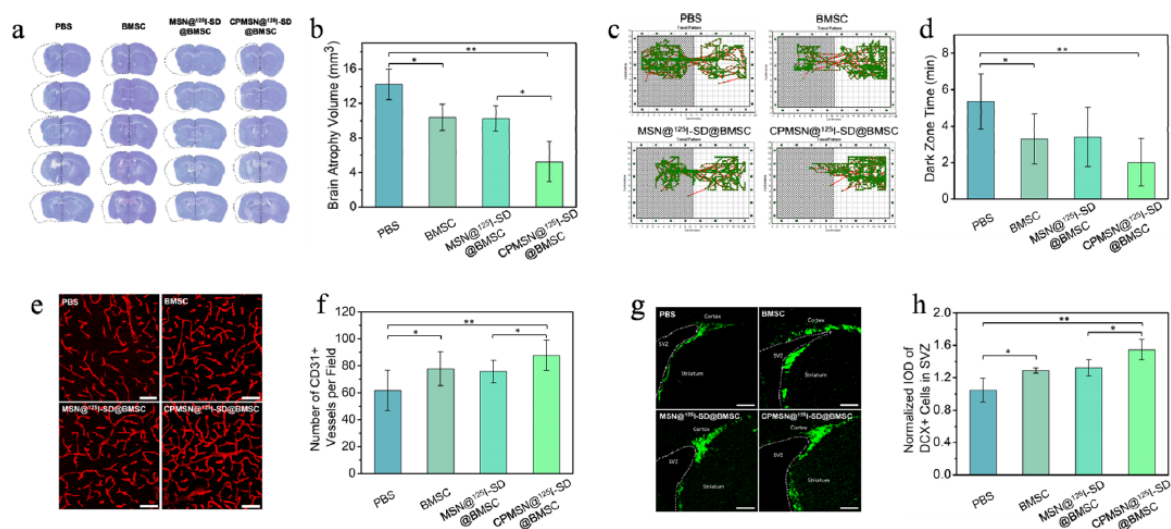


Figure 6. CPMSN@125I-SD-labeled BMSCs attenuate atrophy volume and promote functional recovery. (a,b) Representative images of cresyl-violet-stained brain sections from mice treated with PBS, unlabeled BMSCs, MSN@125I-SD-labeled BMSCs, and CPMSN@125I-SD-labeled BMSCs (a) at 14 days following tMCAO and (b) corresponding atrophy volume. Dashed lines show the border of the atrophy area. (c,d) Smart cage test was used to examine cognitive function at 14 days after tMCAO. (c) Representative images showed a travel pattern of mice in different groups. (d) Time the mice stayed in dark zone was quantified. $n = 10-12$ per group. (e) Photomicrographs showing the CD31+ microvessels in the peri-infarct region for the four groups at 14 days after tMCAO. (f) Bar graph showing the quantification of the number of CD31+ cells. (g) Photomicrographs showing DCX+ neural precursor cells in the SVZ at 14 days after tMCAO. (h) Normalized fluorescence intensity of DCX+ cells in the SVZ (ipsilateral/contralateral hemisphere). IOD, integrated optical density. $n = 6$ per group. Scale bar = 50 μm . CD31, cluster of differentiation 31. DCX, doublecortin; SVZ, subventricular zone. Data are mean \pm SD. * $P < 0.05$; ** $P < 0.01$.

CONCLUSIONS

In summary, a mesoporous core-shell-structured and trimodal theranostic nanoprobe, CPMSN@125I-SD, was fabricated with the aid of microfluidics for labeling BMSCs in brain ischemia treatment. The CPMSN core containing CoPP aggregated within the mesopore channels, which provided a marked enhancement of PA contrast compared to that achieved with free CoPP, thereby enabling the intrinsic monitoring of the BMSC implant in vivo. In addition, the sustained released of CoPP showed an obvious protection effect to BMSCs from oxidative stress. Furthermore, the 125I-labeled SD shell had induced the effective BMSC uptake without influencing the cell viability and also enabled the SPECT imaging, which was significant in long-term quantitative tracking of cell distribution and homing. By intracerebral transplantation of CPMSN@125I-SD-labeled BMSCs in an ischemic stroke mouse model, the brain atrophy was significantly decreased, and the angiogenesis and neurogenesis were tremendously increased, thereby greatly promoting the neurobehavioral recovery. This trimodal theranostic nanoprobe is powerful for both guiding and enhancing stem cell therapy of ischemic stroke.

EXPERIMENTAL METHODS

Chemicals. Cetyltrimethylammonium chloride solution (CTAC, 25 wt % in H_2O), triethanolamine (TEA), dextran (average MW = 9000–11,000), sodium periodate, 4-methylbenzenesulfonate, 2-methoxypropene, spermine, sodium borohydride, pluronic F-127, and sodium hydroxide were purchased from Sigma-Aldrich. Tetraethyl orthosilicate (TEOS) was purchased from Sinopharm Chemical Reagent Co., Ltd. Protoporphyrin IX cobalt chloride (CoPP) was obtained from Frontier Scientific. Dulbecco's modified Eagle's medium (DMEM), FBS, and streptomycin/penicillin were obtained from Gibco Company. All chemicals were used without further purification.

Characterizations. The size distributions and surface zeta potentials of the nanoparticles were measured using the dynamic light scattering method with a ZETASIZER Nano Series (Malvern). Material structures and element mapping images were obtained by TEM (JEM-1400 and JEM-2100F). The surface structures of the nanoparticles were observed under SEM (Hitachi S-4800). The elemental compositions of the nanoparticle powders were evaluated via an XPS (ESCALAB 250). The molar concentrations of Co and Si species in solution were obtained using ICP mass spectrometry (ICP-MS; Agilent 7500ce). LSCM (Zeiss) was used to observe the location of the nanoparticles inside the stem cells. PA imaging was performed with a Vevo LASR imaging system (FUJIFILM Visual Sonics, Inc., USA). The ^1H NMR spectrum of the polymer was recorded at 600 MHz on a Bruker AVANCE III spectrometer. The molecular weight distribution of the polymer was measured using GPC (LC20+RID20A; Shimadzu).

MSN Synthesis. MSNs with large pores were fabricated in a manner similar to that described previously.²⁸ Briefly, 72 mL of deionized water containing 48 mL of CTAC solution (25 wt %) and 0.36 g of TEA were gently stirred at 60 $^\circ\text{C}$ for 1 h. Then, a mixture of cyclohexane (16 mL) and TEOS (4 mL) was added into the CTAC-TEA-water solution under

magnetic stirring at 150 rpm. After reaction for 12 h, the white nanoparticles were collected by centrifugation at 18,000 rpm. Solvent extraction was conducted twice using ammonium nitrate containing anhydrous ethanol at 70 °C to completely remove the template CTAC. Finally, the obtained MSNs were dispersed in anhydrous ethanol for further use. CPMSN Synthesis. To load CoPP in the MSNs, 4 mg of MSNs and a certain amount of CoPP were added to 2 mL of ethanol. The solution was stirred at room temperature for 12 h. After washing with ethanol by centrifugation (18,000 rpm, 10 min) twice, the CPMSN pellets were redispersed in anhydrous ethanol or deionized water by sonication for further use. The CoPP loadings of the MSNs were obtained by the measurement of the Co concentration in a CPMSN water suspension at a mass concentration of 1 mg mL⁻¹ using ICP-MS. Synthesis of Spermine-Modified Acetalated Dextran (SD). SD was synthesized via three steps as follows: The partial oxidation of dextran was performed by mixing 5.0 g of dextran and 1.1 g of sodium periodate in 20 mL of water under magnetic stirring for 5 h at 400 rpm. The polymer was purified by dialysis of the above mixed solution against deionized water with a semipermeable membrane (MWCO, 3500 Da). The complete purification of partially

oxidized dextran was achieved by changing the deionized water five times. The polymer powder was collected by freeze-drying. The partially oxidized dextran thus obtained (3.0 g) was acetalated by reacting with 10.6 mL of 2-methoxypropene and 46.8 mg of 4-methylbenzenesulfonate for 3 h. The reaction was quenched by adding 3 mL of TEA. The polymer was precipitated in 300 mL of deionized water and collected by centrifugation twice at 5000 rpm. The polymer product was lyophilized for the next step of the synthesis. Finally, the partially oxidized acetalated dextran (2.0 g) was reacted with spermine in 10 mL of dimethyl sulfoxide (DMSO) at 50 °C under continuous magnetic stirring for 22 h. Then, 2.0 g of sodium borohydride was added to the DMSO solution. The polymer was precipitated in deionized water and collected by centrifugation at 5000 rpm. The resulting SD was purified by repeated centrifugation (5000 rpm) and washing with water three times. Finally, the collected pellet was lyophilized for further particle fabrication. Microfluidic Fabrication of CPMSN@SD. First, CPMSNs (0.25 mg mL⁻¹) and SD (0.5 mg mL⁻¹) were dispersed in 4 mL of ethanol solution by sonicating for 2 min. Then, an aqueous F127 solution was prepared and its pH was adjusted to about 7.0. The CPMSN/SD/ethanol-containing syringe and the F127-containing syringe were fixed to microfluidic pumps with clamps. The CPMSN/SD/ethanol syringe was connected to the inner capillary of the microfluidic chip and the flow rate was fixed at 2 mL h⁻¹. Meanwhile, the F127 solution syringe was connected to the outer capillary and the flow rate was fixed at 40 mL h⁻¹. The two fluids were mixed at the outlet of the inner capillary to form the core-shell nanoparticles. The final product was obtained by repeated centrifugation (18,000 rpm, 10 min) and washing with 20 mL of deionized water twice. Chemical Conjugation of CPMSN@SD with ¹²⁵I. ¹²⁵I was labelled by using a classical Iodogen-catalyzed method: Na¹²⁵I (200 µCi) was mixed with Iodogen (20 µg) in 50 µL of PBS (0.01 M, pH = 7.4) first and then added into 450 µL of CPMSN@SD suspension (2.5 mg mL⁻¹, pH 7.4) immediately. The suspension was gently vortexed for about 1 min, followed by incubation at 25 °C for 20 min. The labeling efficiency and stability were quantified by radio-thin-layer chromatography (AR2000, Bioscan, USA) using saline as the mobile phase. Free ¹²⁵I was removed by centrifugation (18,000 rpm, 10 min) and washing with 20 mL of deionized water twice. The labeling stability of CPMSN@¹²⁵I-SD was examined in 0.1% FBS solution at 37 °C for 72 h. BMSC Isolation and Labeling. Adult male Sprague-Dawley rats weighing 220–260 g were sacrificed. Femurs and tibias were removed and the ends were snipped off. The bone marrow cavity was washed with sterilized PBS (Hyclone) to collect the cells. The obtained cell suspension was then centrifuged and resuspended in high-glucose DMEM (Hyclone) containing 10% FBS (Gibco, Carlsbad, CA) and 100 U mL⁻¹ penicillin/streptomycin (Gibco, Carlsbad, CA). BMSCs between passages 3 and 5 were used for all experiments. The BMSCs were labeled with CPMSN@¹²⁵I-SD in fresh culture media for different times. After washing with PBS twice, the labeled cells were used for further experiments. To compare the cell labeling efficiencies of CPMSNs and CPMSN@¹²⁵I-SD, the above particles containing the same amount of CPMSNs were added into the BMSC-seeded plates (1,000,000 cells) separately. After incubation for different periods of time, the contents of Si element in the culture medium and inside BMSCs were measured via ICP-OES separately. The samples were measured in parallel (n = 3). The cell labeling efficiency was measured using the below equation: cell labeling efficiency (%) = 100 × (Si content in BMSCs)/(Si content in culture medium + Si content in BMSCs).

Material Cytotoxicity and Antioxidative Stress Evaluation in Vitro. The BMSCs were seeded in 96-well plates at a density of 1 × 10⁴ cells per well. Then, BMSCs were coincubated with different concentrations of CPMSN@¹²⁵I-SD (0–100 µg mL⁻¹) for different times (24 and 48 h). The cell viability was tested with a Cell Counting Kit-8, and the optical density of each well was measured at 450 nm using a microplate reader. The oxidative stress resistances of the BMSCs treated with different labeling agents (CPMSN@¹²⁵I-SD and MSN@¹²⁵I-SD) were evaluated by measuring the LDH release after H₂O₂ (100 µM) treatment for 24 and 48 h. In Vitro Assessment of the PA Imaging Capability of CPMSN@¹²⁵I-SD. Different amounts of CPMSN@¹²⁵I-SD were suspended in PBS (pH 7.4) to obtain final particle suspensions with CoPP concentrations ranging from 0 to 36 µM. Then, 50 µL of each solution was added into a well in solid agarose gel and PA images were obtained using a VEVO LASR imaging system with a 30 MHz transducer at single-laser excitation wavelengths of 680, 745, and 860 nm. To further evaluate the imaging performance of CPMSN@¹²⁵I-SD@BMSC in vivo, a Matrigel/saline (1:1, v/v) suspension containing different numbers of labeled BMSCs (0–2.6 × 10⁵) was subcutaneously injected into the mice. PA imaging was conducted by placing the transducer (30 MHz) onto the injection site, and the average PA intensity of the region of interest (ROI) was read automatically. Establishment of the Transient Middle Cerebral Artery Occlusion Model. All animal research was approved by the Shanghai Jiaotong University Animal Care and Use Committee and performed in accordance with the Guide for Care and Use of Laboratory Animals. First, 48 adult male ICR mice (25–30 g) were randomly divided into four groups (12 mice per group), that is, (1) PBS-treated mice; (2) BMSC-treated mice; (3) MSN@¹²⁵I-SD@BMSC-treated mice; and (4) CPMSN@¹²⁵I-SD@BMSC-treated mice. The mice were anesthetized with 1.5–2% isoflurane and 30/70% oxygen/nitrous oxide. The body temperature was

maintained at 37 ± 0.5 °C using a heating pad. Briefly, the common carotid artery, the internal carotid artery (ICA), and the external carotid artery (ECA) were separated. A 6-0 suture (Covidien, Mansfield, MA, USA) coated with silicon was inserted from the ECA followed by the ICA and gently inserted into the middle cerebral artery (MCA). The success of occlusion was determined by monitoring the decrease in surface cerebral blood flow (CBF) to 10% of baseline CBF using laser Doppler flowmetry (Moor Instruments, Devon, UK). Reperfusion was performed by withdrawing the suture 90 min after transient MCA occlusion (tMCAO). BMSC Transplantation. BMSCs (5×10^5 , 50 μ L) after different treatments were stereotactically injected into the peri-infarct region after 24 h of brain ischemia with the following coordinates: AP: 0.5 mm, L: 1.5 mm ipsilateral to the infarct hemisphere, and V: 2.0 mm using a minipump (WPI, Sarasota, FL) at a rate of 5 μ L min⁻¹. After injection, the needle was maintained for 5 min before withdrawal. The same amount of PBS (50 μ L) was injected as the control. In Vivo PA Imaging and SPECT/CT Imaging of Murine Brain Tissue in the tMCAO Model. For PA imaging, 24 h after tMCAO, mice were anesthetized with 1–2% isoflurane. PA/US images of the murine brains were taken preinjection and immediately after injection of the BMSCs (5×10^5 , 50 μ L) and CPMSN@¹²⁵I-SD@BMSC (5×10^5 , 50 μ L) separately. The images were obtained with a 40 MHz transducer and single laser excitation at 680 nm (2D power: 100%; PA power: 100%; PA gain: 40.0 dB; 2D gain: 25.0 dB). For SPECT/CT imaging, 24 h after tMCAO, mice (n = 4) were intracerebrally injected with CPMSN@¹²⁵I-SD@BMSC (5×10^5) at a radiation dosage of 300 μ Ci. SPECT/CT imaging was performed using a small-animal imaging system with a multipinhole collimator SPECT/CT scanner (Nano SPECT/CT PLUS, Bioscan, USA) from 0 to 8 days postinjection. CT images were used to provide anatomical references to the brain location. The SPECT images were acquired at 32 projections over 360° (radius of rotation = 7.6 cm, 30 s/projection), a 256 \times 256 pixel matrix (1 mm pixel⁻¹), and 26 and 30 keV ¹²⁵I energy windows (20%). Reconstructed data from SPECT and CT were visualized and coregistered using InVivoScope (Bioscan, Washington, DC). The radioactivity of injected cells in vivo was calculated by inviCRO 3D ROIs software.

ACKNOWLEDGMENTS

This work was supported by the National Key R&D Program of China (grant no. 2019YFA0112000), the National Natural Science Foundation of China (grant nos. 81601499, 81801170, and 81671699), the Natural Science Foundation of Shanghai (grant no. 18ZR1444800), the Shanghai Rising-Star Program (grant no. 19QA1410300), the Youth Innovation Promotion Association CAS (grant no. 2020255), and the Academy of Finland (grant no. 328933).

REFERENCES

- (1) Calio', M. L.; Marinho, D. S.; Ko, G. M.; Ribeiro, R. R.; Carbonel, A. F.; Oyama, L. M.; Ormanji, M.; Guirao, T. P.; Calio', P. L.; Reis, L. A.; et al. Transplantation of Bone Marrow Mesenchymal Stem Cells Decreases Oxidative Stress, Apoptosis, and Hippocampal Damage in Brain of a Spontaneous Stroke Model. *Free Radical Biol. Med.* 2014, 70, 141–154.
- (2) Lindvall, O.; Kokaia, Z.; Martinez-Serrano, A. Stem Cell Therapy for Human Neurodegenerative Disorders - How to Make It Work. *Nat. Med.* 2004, 10, S42–S50.
- (3) Li, Y.; Chen, J.; Chen, X. G.; Wang, L.; Gautam, S. C.; Xu, Y. X.; Katakowski, M.; Zhang, L. J.; Lu, M.; Janakiraman, N.; et al. Human Marrow Stromal Cell Therapy for Stroke in Rat - Neurotrophins and Functional Recovery. *Neurology* 2002, 59, 514–523.
- (4) Chen, D.-C.; Lin, S.-Z.; Fan, J.-R.; Lin, C.-H.; Lee, W.; Lin, C.-C.; Liu, Y.-J.; Tsai, C.-H.; Chen, J.-C.; Cho, D.-Y.; et al. Intracerebral Implantation of Autologous Peripheral Blood Stem Cells in Stroke Patients: A Randomized Phase II Study. *Cell Transplant.* 2014, 23, 1599–1612.
- (5) Shyu, W.-C.; Chen, C.-P.; Lin, S.-Z.; Lee, Y.-J.; Li, H. Efficient Tracking of Non-Iron-Labeled Mesenchymal Stem Cells with Serial Mri in Chronic Stroke Rats. *Stroke* 2007, 38, 367–374.
- (6) Hao, L.; Zou, Z. M.; Tian, H.; Zhang, Y. B.; Zhou, H. C.; Liu, L. Stem Cell-Based Therapies for Ischemic Stroke. *BioMed Res. Int.* 2014, 2014, 468748.
- (7) White, B. C.; Sullivan, J. M.; DeGracia, D. J.; O'Neil, B. J.; Neumar, R. W.; Grossman, L. I.; Rafols, J. A.; Krause, G. S. Brain Ischemia and Reperfusion: Molecular Mechanisms of Neuronal Injury. *J. Neurol. Sci.* 2000, 179, 1–33.
- (8) Kim, T.; Lemaster, J. E.; Chen, F.; Li, J.; Jokerst, J. V. Photoacoustic Imaging of Human Mesenchymal Stem Cells Labeled with Prussian Blue-Poly(L-Lysine) Nanocomplexes. *ACS Nano* 2017, 11, 9022–9032.
- (9) Santelli, J.; Lechevallier, S.; Baaziz, H.; Vincent, M.; Martinez, C.; Mauricot, R.; Parini, A.; Verelst, M.; Cussac, D. Multimodal Gadolinium Oxysulfide Nanoparticles: A Versatile Contrast Agent for Mesenchymal Stem Cell Labeling. *Nanoscale* 2018, 10, 16775–16786.
- (10) Dhada, K. S.; Hernandez, D. S.; Suggs, L. J. In vivo Photoacoustic Tracking of Mesenchymal Stem Cell Viability. *ACS Nano* 2019, 13, 7791–7799.
- (11) Kim, T.; Lemaster, J. E.; Chen, F.; Li, J.; Jokerst, J. V. Photoacoustic Imaging of Human Mesenchymal Stem Cells Labeled with Prussian Blue-Poly(L-Lysine) Nanocomplexes. *ACS Nano* 2017, 11, 9022–9032.
- (12) Yin, C.; Wen, G.; Liu, C.; Yang, B.; Lin, S.; Huang, J.; Zhao, P.; Wong, S. H. D.; Zhang, K.; Chen, X.; et al. Organic Semiconducting Polymer Nanoparticles for Photoacoustic Labeling and Tracking of Stem Cells in the Second near-Infrared Window. *ACS Nano* 2018, 12, 12201–12211.
- (13) Nucci, L. P.; Silva, H. R.; Giampaoli, V.; Mamani, J. B.; Nucci, M. P.; Gamarra, L. F. Stem Cells Labeled with Superparamagnetic Iron Oxide Nanoparticles in a Preclinical Model of Cerebral Ischemia: A Systematic Review with Meta-Analysis. *Stem Cell Res. Ther.* 2015, 6, 27.

- (14) Chen, F.; Liu, Y.; Wong, N.-K.; Xiao, J.; So, K.-F. Oxidative Stress in Stem Cell Aging. *Cell Transplant.* 2017, 26, 1483–1495.
- (15) Bernstock, J. D.; Peruzzotti-Jametti, L.; Ye, D.; Gessler, F. A.; Maric, D.; Vicario, N.; Lee, Y.-J.; Pluchino, S.; Hallenbeck, J. M. Neural Stem Cell Transplantation in Ischemic Stroke: A Role for Preconditioning and Cellular Engineering. *J. Cereb. Blood Flow Metab.* 2017, 37, 2314–2319.
- (16) Fu, Y.; Kraitchman, D. L. Stem Cell Labeling for Noninvasive Delivery and Tracking in Cardiovascular Regenerative Therapy. *Expert Rev. Cardiovasc. Ther.* 2010, 8, 1149–1160.
- (17) Chen, F.; Hableel, G.; Zhao, E. R.; Jokerst, J. V. Multifunctional Nanomedicine with Silica: Role of Silica in Nanoparticles for Theranostic, Imaging, and Drug Monitoring. *J. Colloid Interface Sci.* 2018, 521, 261–279.
- (18) Zhang, Y. S.; Wang, Y.; Wang, L.; Wang, Y.; Cai, X.; Zhang, C.; Wang, L. V.; Xia, Y. Labeling Human Mesenchymal Stem Cells with Gold Nanocages for in vitro and in vivo Tracking by Two-Photon Microscopy and Photoacoustic Microscopy. *Theranostics* 2013, 3, 532–543.
- (19) Chen, D.; Dougherty, C. A.; Yang, D.; Wu, H.; Hong, H. Radioactive Nanomaterials for Multimodality Imaging. *Tomography* 2016, 2, 3–16.
- (20) Chaigne, T.; Arnal, B.; Vilov, S.; Bossy, E.; Katz, O. Super-Resolution Photoacoustic Imaging via Flow Induced Absorption Fluctuations. *Optica* 2017, 4, 1397–1404.
- (21) Mallidi, S.; Luke, G. P.; Emelianov, S. Photoacoustic Imaging in Cancer Detection, Diagnosis, and Treatment Guidance. *Trends Biotechnol.* 2011, 29, 213–221.
- (22) Wang, L. V.; Hu, S. Photoacoustic Tomography: In vivo Imaging from Organelles to Organs. *Science* 2012, 335, 1458–1462.
- (23) Wang, X.; Niu, D.; Li, P.; Wu, Q.; Bo, X.; Liu, B.; Bao, S.; Su, T.; Xu, H.; Wang, Q. Dual-Enzyme-Loaded Multifunctional Hybrid Nanogel System for Pathological Responsive Ultrasound Imaging and T₂-Weighted Magnetic Resonance Imaging. *ACS Nano* 2015, 9, 5646–5656.
- (24) Chen, L.; Chen, J. Y.; Qiu, S. S.; Wen, L.; Wu, Y.; Hou, Y.; Wang, Y.; Zeng, J. F.; Feng, Y.; Li, Z.; et al. Biodegradable Nanoagents with Short Biological Half-Life for SPECT/PAI/MRI Multimodality Imaging and PTT Therapy of Tumors. *Small* 2018, 14, 1702700.
- (25) Thawani, J. P.; Amirshaghghi, A.; Yan, L. S.; Stein, J. M.; Liu, J.; Tsourkas, A. Photoacoustic-Guided Surgery with Indocyanine Green-Coated Superparamagnetic Iron Oxide Nanoparticle Clusters. *Small* 2017, 13, 1701300.
- (26) Kraitchman, D. L.; Gilson, W. D.; Lorenz, C. H. Stem Cell Therapy: MRI Guidance and Monitoring. *J. Magn. Reson. Imaging* 2008, 27, 299–310.
- (27) Boss, A.; Weiger, M.; Wiesinger, F. Future Image Acquisition Trends for PET/MRI. *Semin. Nucl. Med.* 2015, 45, 201–211.
- (28) Shen, D.; Yang, J.; Li, X.; Zhou, L.; Zhang, R.; Li, W.; Chen, L.; Wang, R.; Zhang, F.; Zhao, D. Biphasic Stratification Approach to Three-Dimensional Dendritic Biodegradable Mesoporous Silica Nanospheres. *Nano Lett.* 2014, 14, 923–932.
- (29) Chen, Z.; Krishnamachary, B.; Penet, M.-F.; Bhujwalla, Z. M. Acid-Degradable Dextran as an Image Guided Sirna Carrier for Cox-2 Downregulation. *Theranostics* 2018, 8, 1–12.
- (30) Cohen, J. L.; Schubert, S.; Wich, P. R.; Cui, L.; Cohen, J. A.; Mynar, J. L.; Frechet, J. M. J. Acid-Degradable Cationic Dextran Particles for the Delivery of Sirna Therapeutics. *Bioconjugate Chem.* 2011, 22, 1056–1065.
- (31) Bachelder, E. M.; Beaudette, T. T.; Broaders, K. E.; Dashe, J.; Frechet, J. M. J. Acetal-Derivatized Dextran: An Acid-Responsive Biodegradable Material for Therapeutic Applications. *J. Am. Chem. Soc.* 2008, 130, 10494–10495.
- (32) Xia, T.; Kovichich, M.; Liong, M.; Meng, H.; Kabehie, S.; George, S.; Zink, J. I.; Nel, A. E. Polyethyleneimine Coating Enhances the Cellular Uptake of Mesoporous Silica Nanoparticles and Allows Safe Delivery of Sirna and DNA Constructs. *ACS Nano* 2009, 3, 3273–3286.
- (33) Albukhaty, S.; Naderi-Manesh, H.; Tiraihi, T. In vitro Labeling of Neural Stem Cells with Poly-L-Lysine Coated Super Paramagnetic Nanoparticles for Green Fluorescent Protein Transfection. *Iran. Biomed. J.* 2013, 17, 71–76.
- (34) Tan, Z.; Lan, W.; Liu, Q.; Wang, K.; Hussain, M.; Ren, M.; Geng, Z.; Zhang, L.; Luo, X.; Zhang, L.; et al. Kinetically Controlled Self-Assembly of Block Copolymers into Segmented Wormlike Micelles in Microfluidic Chips. *Langmuir* 2019, 35, 141–149.
- (35) Liu, D.; Zhang, H.; Ma "kila", E.; Fan, J.; Herranz-Blanco, B.; Wang, C.-F.; Rosa, R.; Ribeiro, A. J.; Salonen, J.; Hirvonen, J.; et al. Microfluidic Assisted One-Step Fabrication of Porous Silicon@Acetalated Dextran Nanocomposites for Precisely Controlled Combination Chemotherapy. *Biomaterials* 2015, 39, 249–259.
- (36) Williams, A. R.; Hare, J. M. Mesenchymal Stem Cells. *Circ. Res.* 2011, 109, 923–940.
- (37) Liu, Y.; Bhattarai, P.; Dai, Z.; Chen, X. Photothermal Therapy and Photoacoustic Imaging via Nanotheranostics in Fighting Cancer. *Chem. Soc. Rev.* 2019, 48, 2053–2104.
- (38) Jiang, Y. Y.; Pu, K. Y. Advanced Photoacoustic Imaging Applications of Near-Infrared Absorbing Organic Nanoparticles. *Small* 2017, 13, 1700710.
- (39) Yao, M.; Ma, M.; Zhang, H.; Zhang, Y.; Wan, G.; Shen, J.; Chen, H.; Wu, R. Mesopore-Induced Aggregation of Cobalt Porphyrin for Photoacoustic Imaging and Antioxidant Protection of Stem Cells. *Adv. Funct. Mater.* 2018, 28, 1804497.

- (40) Aghayan, H. R.; Soleimani, M.; Goodarzi, P.; Norouzi-Javidan, A.; Emami-Razavi, S. H.; Larijani, B.; Arjmand, B. Magnetic Resonance Imaging of Transplanted Stem Cell Fate in Stroke. *J. Res. Med. Sci.* 2014, 19, 465–471.
- (41) Nam, S. Y.; Ricles, L. M.; Suggs, L. J.; Emelianov, S. Y. In vivo Ultrasound and Photoacoustic Monitoring of Mesenchymal Stem Cells Labeled with Gold Nanotracers. *PLoS One* 2012, 7, No. e37267.
- (42) Kubelick, K. P.; Snider, E. J.; Ethier, C. R.; Emelianov, S. Development of a Stem Cell Tracking Platform for Ophthalmic Applications Using Ultrasound and Photoacoustic Imaging. *Theranostics* 2019, 9, 3812–3824.
- (43) Bulte, J. W. M.; Daldrup-Link, H. E. Clinical Tracking of Cell Transfer and Cell Transplantation: Trials and Tribulations. *Radiology* 2018, 289, 604–615.
- (44) Ma, M.; Shu, Y.; Tang, Y.; Chen, H. Multifaceted Application of Nanoparticle-Based Labeling Strategies for Stem Cell Therapy. *Nano Today* 2020, 34, 100897.
- (45) Nguyen, P. K.; Riegler, J.; Wu, J. C. Stem Cell Imaging: From Bench to Bedside. *Cell Stem Cell* 2014, 14, 431–444.
- (46) Zhu, S.-z.; Szeto, V.; Bao, M.-h.; Sun, H.-s.; Feng, Z.-p. Pharmacological Approaches Promoting Stem Cell-Based Therapy Following Ischemic Stroke Insults. *Acta Pharmacol. Sin.* 2018, 39, 695– 712.
- (47) Bang, O. Y.; Kim, E. H.; Cha, J. M.; Moon, G. J. Adult Stem Cell Therapy for Stroke: Challenges and Progress. *J. Stroke* 2016, 18, 256–266.
- (48) Baraniak, P. R.; McDevitt, T. C. Stem Cell Paracrine Actions and Tissue Regeneration. *Regener. Med.* 2010, 5, 121–143.
- (49) Ruan, L.; Wang, B.; ZhuGe, Q.; Jin, K. Coupling of Neurogenesis and Angiogenesis after Ischemic Stroke. *Brain Res.* 2015, 1623, 166–173.